Dalton Transactions

PAPER

View Article Online
View Journal | View Issue

Cite this: *Dalton Trans.*, 2016, **45**, 18954

Approaching the size limit of organometallic layers: synthesis and characterization of highly ordered silver–thiolate lamellae with ultra-short chain lengths†

Zichao Ye,[a,b] Lito P. de la Rama,[a,b] Mikhail Y. Efremov,[c] Jian-Min Zuo[a] and Leslie H. Allen*[a,b]

Received 19th September 2016,
Accepted 31st October 2016

DOI: 10.1039/c6dt03629e

www.rsc.org/dalton

Approaching the ultimate limits of material sizes provides a route for designing new functional materials with extraordinary properties. We report the first systematic synthesis and characterization study of a wide range of highly ordered silver alkanethiolate ($AgSC_nH_{2n+1}$ or AgSC*n*, *n* = 1–16) aliphatic lamellae. Single crystalline multilayer AgSC*n* are synthesized by a modified solution reaction method. Hot toluene recrystallization or Ostwald ripening enhances the structural ordering of the lamellar crystals. This work approaches the chain length limit of aliphatic lamellae by synthesizing highly ordered AgSC*n* (*n* = 1–3) with extremely short chains. All lamellae form single crystals with well-registered interlayer interfaces, similar to other alkyl-based lamellae but different from polyethylene lamellae. AgSC2 with a layer thickness of 1.08 nm is the thinnest organometallic layer ever reported. The composition, morphology, decomposition and structure of the lamellae are comprehensively studied. A new method quantifies the composition of the residual Ag and Ag_2S contents after the decomposition of the AgSC*n*: all of the Ag, none of the C and a fraction of the S remain in the residue. The structural orderings of the AgSC*n* crystals, which are probed by electron diffraction for the first time, are characterized in terms of chain conformation, interlayer lamellar ordering and intralayer lattice ordering. All AgSC*n* (*n* = 2–16) layers, except AgSC1, possess a common lattice packing and the same inorganic network structure.

Introduction

As a "golden nugget" for nanoscience, materials exhibit extraordinary properties when their dimensions approach ultimate scale limits. Graphene shows remarkably high electrical conductivity as compared with its "multilayer parent", graphite.[1] Indium nanoparticles show discrete "magic size" melting when their radii are smaller than 10 nm.[2,3] The quantum-size effect predicts the opening of band gaps in metal particles with decreased sizes.[4]

Metal–thiolate lamellae[5–28] are currently of increasing scientific and technological interest, which has arisen from the other two more widely studied organometallic systems: self-assembled monolayers (SAM)[29–33] and monolayer protected clusters (MPC or 3D SAM).[34–37] The two-dimensional (2D) nanoconfinement of metal-aliphatic layers is fostering potential applications in lithography,[38] nanoelectronics,[39] biophysics[40] and liquid crystals.[6]

Size-dependent melting of silver alkanethiolate ($AgSC_nH_{2n+1}$ or AgSC*n*) layers has been recently studied for species with $n \geq 7$.[20] However, extremely thin AgSC*n* sheets with ultra-short chain lengths ($n \leq 6$, especially n = 1–3), where nontrivial properties might occur, are rarely studied. It is difficult to synthesize these crystals with highly ordered lamellar structures. This work is inspired by the well-known strategy of approaching graphene from graphite by exfoliating carbon layers.[1] In a close analogy with exfoliation, a gradual shortening of the aliphatic chain length in AgSC*n* opens a route toward the lamella-thickness-limit of organometallic layers, as illustrated in Fig. 1. This methodology paves the way toward species (*e.g.* AgSC1, AgSC2) that have unique properties at ultimate scales. This top-down strategy might eventually yield a

[a]*Department of Materials Science and Engineering, Frederick-Seitz Materials Research Laboratory, University of Illinois at Urbana-Champaign, Urbana, Illinois 61801, USA. E-mail: l-allen9@illinois.edu*
[b]*Coordinated Science Laboratory, University of Illinois at Urbana-Champaign, Urbana, Illinois 61801, USA*
[c]*College of Engineering, University of Wisconsin-Madison, Madison, Wisconsin 53706, USA*

† Electronic supplementary information (ESI) available: Some additional characterization results, including elemental analysis, SEM, XRD, DSC, FTIR and SAED. A schematic of the structure of the material studied. See DOI: 10.1039/c6dt03629e

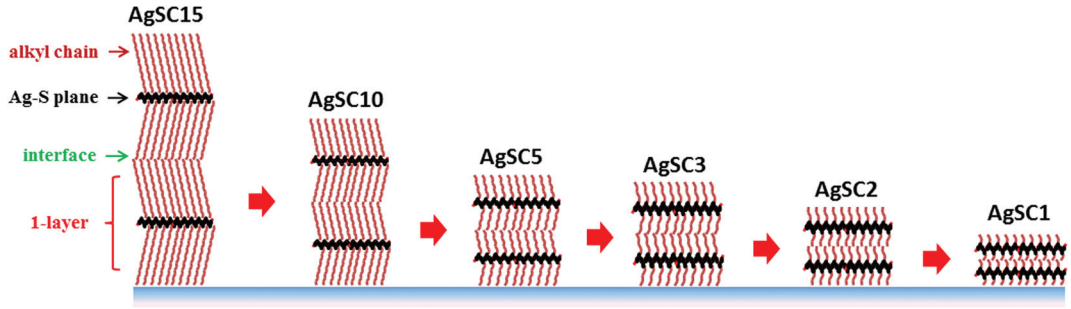

Fig. 1 Schematic shows the methodology used in this research. The ultimate size limit of AgSC*n* lamellae is approached by gradually shortening their chain lengths from AgSC15 to AgSC1. A single layer AgSC*n* is composed of an Ag–S central plane with alkyl chains extending both sides. Interlayer interfaces are formed between adjacent layers.

novel 2D Ag–S sheet, similar to the 2D materials of transition metal dichalcogenides.[41]

A single layer AgSC*n* is composed of a 2D Ag–S central plane with fully extended alkyl chains on both sides (Fig. 1).[5,15,19] Within a layer (intralayer), parallel chains interact with each other *via* van der Waals forces. Multiple 1-layer crystals can stack into multilayer lamellae, with interlayer van der Waals forces connecting adjacent layers, forming interfaces. AgSC*n* lamellae are essentially members of 2D van der Waals layered materials,[19,23,42] among which graphene,[1] MoS_2 [43] and Bi_2Se_3 [44] are some typical examples of growing interest.

AgSC*n* lamellae have been synthesized by two routes. Method-1: solution reaction between metal salts and alkanethiols, initiated by Dance *et al.*;[5] Method-2 (vapor-grown method): surface reaction between silver clusters and thiol vapors, developed by Hu *et al.*[18,19] Their products are equivalent in terms of composition, morphology, lamellar structure and chain conformation. Most of the lamellae studied so far were long chain AgSC*n* with $n \geq 7$.[8,12,14,15,18–21] Levchenko *et al.*[15] dramatically improve the crystallinity of lamellae *via* hot solution recrystallization. However, highly ordered layers of short chain species ($n < 7$) have never been obtained and characterized, let alone ultrathin lamellae of AgSC1 and AgSC2 with extremely short chains. The only reported short chain AgSC*n* (n = 3, 4, 6) lamellae[5,7] possess relatively low orderings, as compared with the recrystallized long chain crystals.[15] Short chain metal–thiolates tend to form crystals with disordered interlayer interfaces.[16] Such examples also include short chain gold alkanethiolates (AuSC*n*, n = 2–7),[16] palladium alkanethiolates ($Pd(SCn)_2$, n = 4, 6)[13] and Nickel alkanethiolates ($Ni(SCn)_2$, n = 4).[24]

This work reports the first systematic synthesis and characterization of a wide range of highly ordered AgSC*n* (n = 1–16) that includes both short and long chain lamellae of either chain parity. It completes the study of the AgSC*n* family by probing species that have been missed in prior works.[5–8,10–12,14,15] A new synthesis pathway improves the structure ordering of the crystals. AgSC1 is the first obtained well-ordered aliphatic lamellae with only one carbon attached to the inorganic backbone. AgSC2 is the thinnest organometallic layer ever reported. The composition, morphology and decomposition of AgSC*n* are comprehensively characterized. The structures of the lamellae are studied in terms of aliphatic chain conformation, interlayer lamellar registration and intralayer lattice ordering. This work is instructive for studying the structure of biological membranes,[40] single layer electronics[19,39] as well as synthesis method using thiolates as intermediate reagents.[26]

Experimental

AgSC*n* (n = 1–16) synthesis

Materials. The following chemicals are purchased from Sigma-Aldrich Co. and used without further purification: silver nitrate powder ($AgNO_3$, ≥99.0%), acetonitrile (99.8%), triethylamine (≥99.0%), sodium methanethiolate ($NaSCH_3$, ≥95%) and 1-alkanethiols with various chain lengths (1-$C_nH_{2n+1}SH$, n = 2–16, except for n = 13, ≥98%). Toluene (≥99.5%) is used as received from Macron Fine Chemicals Co.

Synthesis. The multilayer AgSC*n* (n = 1–16) crystals in this work are synthesized using a modified solution reaction method (Method-3). The original solution synthesis pathway (Method-1) has been employed to synthesize various metal–thiolates.[5,9,13,16,17] Method-3 has two critical modifications as compared with Method-1, leading to more complete reactions: (1) the molar ratios of the starting $AgNO_3$ and thiol source (1-$C_nH_{2n+1}SH$ or $NaSCH_3$) are set to be 1 : 2 (*i.e.* excess thiols), rather than equimolar; (2) the reaction time is extended to be 24 h. AgSC*n* (n = 2–16) crystals precipitate out when gradually adding an $AgNO_3$ (1 mmol) acetonitrile (15 ml) solution, at a rate of 1 ml min^{-1}, into another acetonitrile (30 ml) solution of 1-alkanethiol (2 mmol) and trimethylamine (2 mmol). The mixture is stirred for 1 day without light exposure. The precipitates are separated from the liquid phase using vacuum filtration and washed with acetonitrile. AgSC1 is synthesized by the same procedure using $NaSCH_3$ salt, instead of gaseous CH_3SH.[45] The mechanism of the synthesis is suggested elsewhere[15] and the overall reactions are expressed as follows:

$$AgNO_3 + C_nH_{2n+1}SH + (C_2H_5)_3N \rightarrow AgSC_nH_{2n+1}\ (n = 2-16)\downarrow + [(C_2H_5)_3NH]NO_3 \quad (1)$$

$$AgNO_3 + NaSCH_3 \rightarrow AgSCH_3\downarrow + NaNO_3 \quad (2)$$

Inspired by the post-reaction recrystallization method used for long chain AgSC*n* ($n \geq 10$),[15] all precipitates in this work are recrystallized or Ostwald ripened in hot toluene. 10 ml toluene (b.p. 111 °C) at 100–105 °C easily dissolve 1 mmol as-synthesized AgSC*n* (n = 4, 6–16) within seconds, forming transparent yellow solutions. However, the same amount of AgSC*n* (n = 1–3) and AgSC5 stays as precipitates or forms suspension, respectively, in toluene under the same conditions. Vigorous stirring of such two-phase mixtures for 5–10 min stimulates Ostwald ripening of the crystals (n = 1–3, 5). Both solutions (n = 4, 6–16) and mixtures (n = 1–3, 5) are passively cooled down to room temperature. Precipitated crystals are filtered, washed in acetonitrile and dried in air overnight. All the final AgSC*n* (2–16) crystals are white powders, except that AgSC1 is yellow.

Characterization of AgSC*n* (n = 1–16)

Elemental analysis. The contents of C and H in AgSC*n* are characterized in an Exeter Analytical CE 440 CHN Analyzer. The contents of Ag and S are measured in a PerkinElmer 2000DV optical emission spectrometer with inductively coupled plasma.

Scanning electron microscopy (SEM). The morphology of AgSC*n* crystals is studied by using a Hitachi S4700 SEM with an accelerating voltage of 15 kV.

Thermogravimetric analysis (TGA). The decomposition properties of AgSC*n* powders are studied in a TA-Q50 TGA analyzer. All the experiments are conducted under a N_2 atmosphere from room temperature to 500 °C, at a heating rate of 10 °C min^{-1}.

Powder X-ray diffraction (XRD). Powder XRD measurements are done in a Siemens D5000 diffractometer using Cu-Kα radiation (λ = 1.5418 Å, 40 kV, 30 mA). XRD patterns are acquired by 2θ scanning at a rate of 1° min^{-1} and a step size of 0.02°. Samples are packed in a well of a standard sample holder. The raw patterns are fitted *via* JADE-9 X-ray analysis software. Interlayer spacings of lamellae are automatically calculated using Bragg's Law.

Fourier transform infrared spectroscopy (FTIR). The conformational order of alkyl chains in AgSC*n* are studied by using a Thermo Nicolet Nexus 670 FTIR. Samples are prepared by drop-casting AgSC*n*–acetonitrile suspensions on Si substrates. Absorbance spectra (1175–3100 cm^{-1}) are collected with a spectral resolution of 2 cm^{-1} and the signal-to-noise ratio is enhanced by averaging over 128 scans.

Transmission electron microscopy (TEM) and selected area electron diffraction (SAED). A JEOL 2100 TEM is employed at 200 kV to study the morphology and the single crystal electron diffractions of AgSC*n*. AgSC*n*–acetonitrile suspensions are drop-cast on holey carbon membranes for sample preparation. Beam current is set very low (~1–2 pA cm^{-2}) to slow down the degradation of AgSC*n* crystals under e-beam exposure.[18]

Differential scanning calorimetry (DSC). The melting properties of AgSC3 and Ag_2S powders are measured using a PerkinElmer Standard Single-Furnace DSC-4000 with aluminum sample pans. The heating and cooling rates are set to be 10 °C min^{-1}. The instrument is calibrated using indium and zinc.[21] Experiments are conducted in a N_2 environment. The heat capacity (C_p) of the sample is calculated by dividing the heat flow by the scanning rate. The obtained calorimetric curves are used to determine the melting temperature (peak position) and melting enthalpy (peak area) of the samples.

Results

Composition and morphology of thiolates

Mass fractions of C, H, Ag and S in the thiolates, determined by elemental analysis, are consistent with the formulae $AgSC_nH_{2n+1}$ (n = 1–16) within experimental error (Table SI-I;† C: ±0.4%, H: ±0.2%, S: ±0.9%, Ag: ±2%). The composition of AgSC*n* is visualized in Fig. 2. The sum of the percentages of the four elements is 100 ± 2% for each sample, indicating that pure AgSC*n* crystals are formed. No N (<0.1%) is detected, which eliminates possible contamination of the products by the nitrate, solvent (CH_3CN) or trimethylamine. The purity of our products is similar to that of AgSC12 and AgSC4 synthesized by Method-1.[7,8]

SEM images of AgSC*n* lamellae are illustrated in Fig. 3 (n = 1–7) and Fig. SI-1† (n = 8–16). All AgSC*n* crystals are clearly recognized to be nanosheets with low aspect ratios and well-defined crystal facets and shapes. Some flakes are thin enough to be transparent. The estimated sheet thicknesses are 100–500 nm. In contrast, the lamellar morphology of AgSC12 layers synthesized from Method-1 is reported to be unrecognizable, as crystals aggregate into bulky chunks.[8] Our synthesis route prevents crystal aggregation such that large single crystals are easily separated.

Notably, Fig. 3b shows two perpendicularly grown AgSC1 flakes, which is not observed for other AgSC*n* species. This is

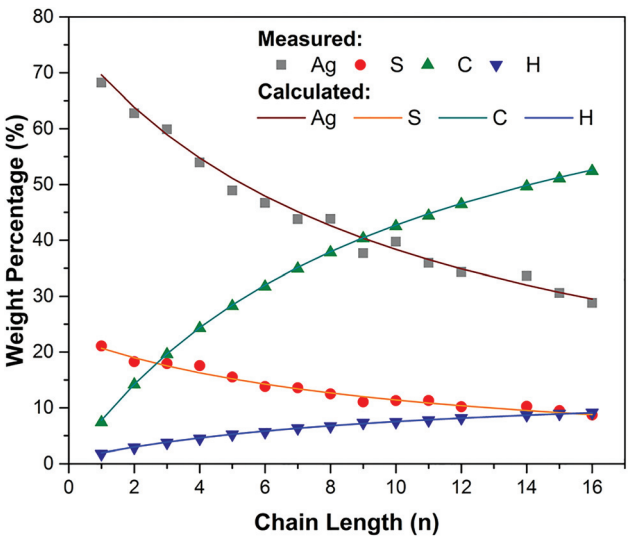

Fig. 2 Plot visualizes the elemental weight percentages of Ag, S, C and H in AgSC*n* (n = 1–16). Both measured and formulae calculated compositions are shown. Raw data are summarized in Table SI-I.†

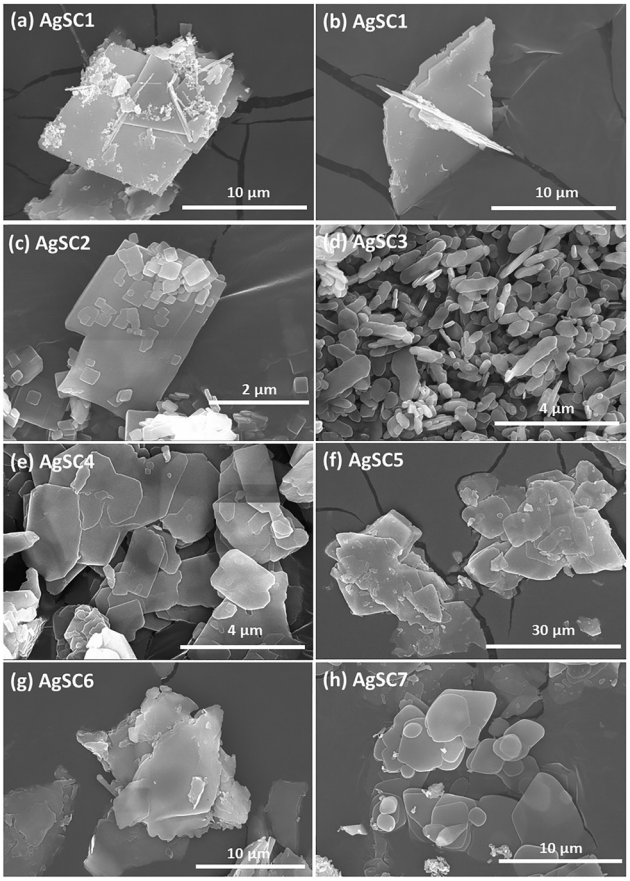

Fig. 3 SEM images of multilayer (a, b) AgSC1, (c) AgSC2, (d) AgSC3, (e) AgSC4, (f) AgSC5, (g) AgSC6 and (h) AgSC7 lamellar crystals with well-defined shapes and low aspect ratios. Image (b) illustrates two perpendicularly positioned AgSC1 flakes.

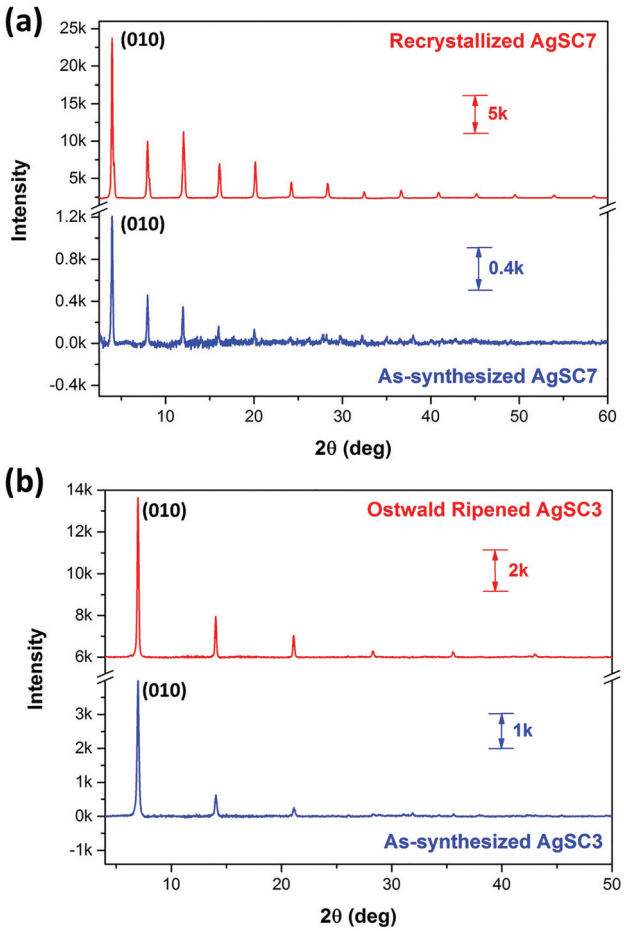

Fig. 4 Comparisons between the XRD patterns of as-synthesized and hot toluene processed (a) AgSC7 (recrystallized) and (b) AgSC3 (Ostwald ripened) lamellar crystals. All the peaks shown represent (0*k*0) reflections.

the evidence of the uniqueness of AgSC1 structure that is discussed in later sections.

Post-reaction processing of AgSC*n*

Post-reaction processing in hot toluene enhances lamellar ordering of AgSC*n*, as suggested by Levchenko *et al.* for $n \geq 10$ (ref. 15) and reproduced in this work for a broader range of chain lengths (n = 1–16).

Fig. 4a and b reveal the effect of hot toluene processing on the crystallinity of AgSC7 (recrystallization) and AgSC3 (Ostwald ripening), respectively. Sample preparation ensures the validity of a similar volume (mass) assumption necessary for quantitative analysis. XRD (0*k*0) reflections of as-synthesized and hot toluene processed AgSC*n* show equal layer spacings, but their patterns have several major differences (Table SI-II†): (1) the Full-Width-Half-Maximum (FWHM) of the (0*k*0) lamellar peaks is narrower for the recrystallized or ripened samples, which, based on the Scherrer equation, indicates that the hot toluene processing promotes layer stacking and helps form thicker crystals; (2) the integrated intensity of the (010) peak increases more than 10 times after recrystallization (AgSC7) and slightly (1.6 times) after Ostwald ripening (AgSC3); (3) more orders of (0*k*0) diffractions with better signal-to-noise ratio are observed for the recrystallized or ripened crystals. The larger increase in the crystallinity of AgSC7 (Fig. 4a) as compared with that of AgSC3 (Fig. 4b) is expected since AgSC7 dissolves in hot toluene while AgSC3 does not (see Experimental).

Given the material amount and the experimental setup that are used in this work, the integrated intensity of specific XRD peaks is proportional to the effective volume of crystalline materials in the powder sample.[46] Therefore, recrystallization or Ostwald ripening increases the total portion of well-crystallized lamellar structures that produce strong (0*k*0) signals. Prior works[47–49] mentioned that reduced diffraction intensity and number of orders are indicators of increased layer thickness fluctuations, and the higher-order peaks are more sensitive to such fluctuations. We infer that the recrystallized or ripened AgSC*n* lamellae have smaller layer roughness, and thus adjacent layers are well-registered at interlayer interfaces, as compared with that of as-synthesized samples.

Synthesis of well-ordered AgSC1 and AgSC2 lamellae

Due to the difficulty of controlling CH_3SH gas (all other alkanethiols are either liquid or solid at room temperature), $NaSCH_3$ is employed alternatively as the thiol source for synthesizing AgSC1. The use of alkanethiol or its corresponding sodium salt is equivalent as a reactant. To prove this conclusion, a control experiment is done to compare AgSC3 lamellae synthesized from either C_3H_7SH or $NaSC_3H_7$. The products are found to be equivalent in terms of composition, lamellar structure, morphology and melting properties.

Fig. 5 and SI-2† illustrate the XRD (0k0) lamellar reflections of short chain (n = 1–5) and long chain AgSCn (n = 6–16), respectively. AgSC1 (11.94 ± 0.01 Å) is the first studied thiolate lamellae with only one methyl group attached to the inorganic backbone, whereas AgSC2 lamellae have the thinnest layer thickness of 10.77 ± 0.01 Å among the AgSCn family. To our knowledge, 1.08 nm is the thinnest organometallic lamellae ever reported. For comparison, the thinnest species of other studied organometallic layers are as follows: AuSCn (n = 4, t_{min} ~ 1.6 nm),[16] Pd(SCn)$_2$ (n = 6, t_{min} ~ 1.8 nm),[13,39] Ni(SCn)$_2$ (n = 4, t_{min} ~ 1.4 nm),[24] copper alkanethiolate CuSCn (n = 4, t_{min} ~ 1.6 nm),[9] silver arenethiolate (AgSPh, t_{min} ~ 1.4 nm)[5] and silver carboxylate $AgO_2CC_{n-1}H_{2n-1}$ (n = 2, t_{min} ~ 2.1 nm).[50] The layer thickness of AgSC2 is also smaller than that of AgSC1, due to their different lattice packings (see later sections).

All the diffraction patterns (Fig. 5, SI-2†) with n = 2–16 present 7 or more lamellar peaks; even AgSC1 shows 5 orders of lamellar diffractions. Extremely short chain thiolates with highly ordered lamellar structures are usually difficult to synthesise. The only reported XRD results for short chain AgSCn (n = 3, 4, 6)[5,7] show at most 4 orders of lamellar reflections. A similar XRD analysis was reported for AuSCn,[16] Pd(SCn)$_2$[13] and Ni(SCn)$_2$,[24] whose layer orderings decrease significantly as chain length decreases. These short chain thiolates (Au, Pd, Ni) are claimed to have rougher interfaces with poorer interlayer registry than their long chain counterparts.[13,16,24]

In contrast, our synthesis produces AgSCn with highly ordered interfaces over the entire range of chain lengths (n = 1–16).

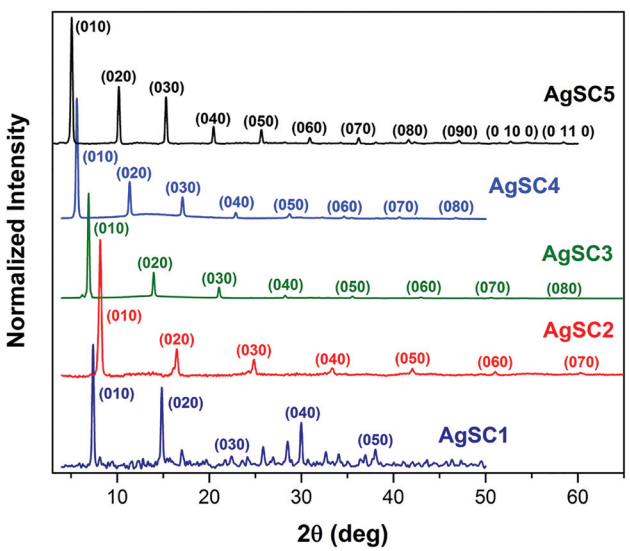

Fig. 5 XRD patterns of short chain AgSCn (n = 1–5) with well-defined lamellar ordering.

Thermal decomposition of thiolates

TGA curves are illustrated in Fig. 6a for both short and long chain AgSCn (n = 1–6, 8, 11, 15). All the lamellae show similar irreversible decomposition profiles with onset temperatures (T_{onset}) between 210–230 °C. This result is consistent with other researchers' work on long chain AgSCn (n = 10, 12, 16, 18), where T_{onset} = ~220 °C.[15] But they did not report a T_{onset} trend due to the limited range of chain lengths investigated.[15]

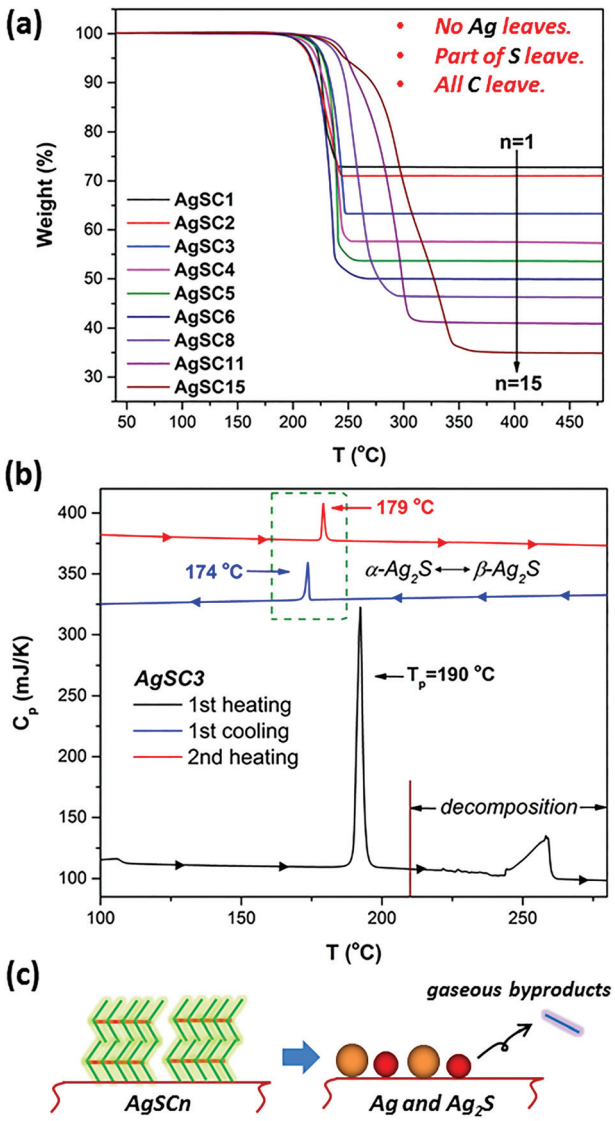

Fig. 6 (a) TGA curves for AgSCn (n = 1–6, 8, 11, 15) with T_{onset} between 210–230 °C. (b) DSC traces (heating, cooling, reheating) to 280 °C for AgSC3. (c) Schematic shows the suggested procedure of AgSCn decomposition, with Ag and Ag_2S as residues.

We found a slight but progressive increase of T_{onset} as chain length increases (n = 1–16). This trend is attributed to the increase in cohesive interactions among alkyl groups as chain length increases,[15] and agrees with the reported data on the decomposition of AuSCn.[16]

Residue materials after TGA are mixtures of Ag and Ag_2S, whereas unlike Garcia-Barrasa *et al.*'s work,[26] no di-*n*-alkyl-disulfide lamellae are observed. This conclusion agrees with prior results[15] and is verified by XRD (Fig. SI-3†). Reflection peaks of Ag (111), Ag (200), Ag_2S ($\bar{1}12$) and Ag_2S (121) are observed. Ag_2S is also identified by DSC measurements of the residues, as is shown in Fig. 6b for AgSC3. The 1st heating curve shows its melting peak (~190 °C)[51] and the decomposition range beyond 210 °C. Subsequent DSC traces present the phase transition of residual materials. Peaks at 174 °C for the 1st cooling trace and at 179 °C for the 2nd heating trace are observed (5 °C of supercooling). This peak agrees with that of the solid–solid phase transition between room-temperature-stable α-Ag_2S (acanthite) and high-temperature-stable β-Ag_2S (argentite), and is measured by earlier works to be 176–180 °C.[52–54]

The Ag and Ag_2S contents in the residue are calculated by two methods. The first method directly computes their ratio from the weight loss determined by TGA (*e.g.* AgSC3 residue: 49.9% Ag, 51.1% Ag_2S). The second method estimates the Ag_2S content based on the enthalpy of the solid phase transition in Fig. 6b (*e.g.* AgSC3 residue: 49.1% Ag, 50.9% Ag_2S). The molar enthalpy for commercial Ag_2S is measured to be 4.20 ± 0.03 kJ mol^{-1} under the same DSC conditions (Fig. SI-4†). The results of both methods are consistent. This is the first time that the decomposition residues of metal–thiolates have been quantified.

We conclude that the decomposition of solid-state AgSCn is accompanied by the cleavage of S–C and Ag–S bonds, leaving all of the Ag, part of the S and none of the C in the residue (Fig. 6c). In the case of AgSC3, ~23% of the S content remains in the residue. However, Ag_2S is absent under some other decomposition conditions.[26]

Structures of AgSCn

Structures of AgSCn (n = 1–16) in this work possess a highly ordered molecular arrangement, even for extremely short chain species. Such ordering is systematically characterized in terms of alkyl chain conformation, interlayer lamellar registration and intralayer lattice ordering.

Conformational order of polymethylene chains. FTIR is employed to study the chain conformational order of AgSCn lamellae, following prior works.[10,11,18] Fig. 7a shows the FTIR spectra of AgSCn (n = 1–16) crystals for the C–H stretching region (2750–3000 cm^{-1}). Peak positions of CH_2 stretching modes are sensitive indicators of chain ordering.[55–57] The symmetric ($\nu_s(CH_2)$, d$^+$) and anti-symmetric ($\nu_{as}(CH_2)$, d$^-$) stretching modes of CH_2 groups are located at 2845–2851 cm^{-1} and 2915–2920 cm^{-1}, respectively, for n = 4–16, indicating all-*trans* extended polymethylene chains. Based on prior works,[58–62] the

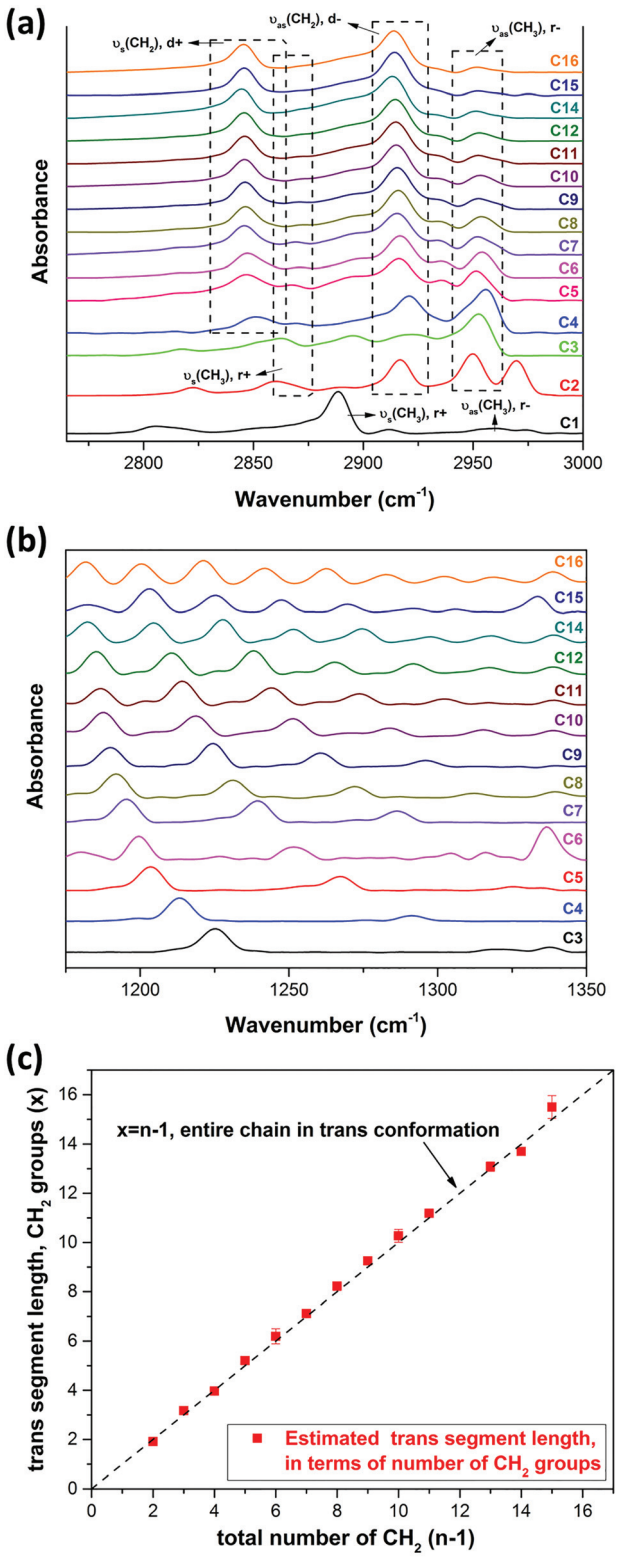

Fig. 7 FTIR spectra of AgSCn (n = 1–16) lamellae at (a) high-frequency (2750–3000 cm^{-1}) and (b) low-frequency (1175–1350 cm^{-1}) regions. (c) Plot shows the *trans* segment length of alkyl chains, in terms of number of CH_2 groups, as a function of the total number (n – 1) of CH_2 groups in AgSCn (n = 3–16).

d^+ and d^- peaks shift to 2854–2856 cm^{-1} and 2924–2928 cm^{-1}, respectively, when the population of *gauche* conformers increases. Analogous to the CH_2 stretching spectrum of 3D-SAM (n = 3),[57] no d^+ but only d^- mode (2923 cm^{-1}) is observed for AgSC3. AgSC3 shows more *gauche* defects along the chains than that of AgSCn (n = 4–16). No *trans* or *gauche* conformer is defined for AgSC1 and AgSC2.

The integrated intensity ratio of d^- and d^+ peaks is an indicator of chain disorder.[22,58,61–63] An increasing ratio of I_{2915}/I_{2845} (I_{d^-}/I_{d^+}) implies a decreasing conformational order. Fig. SI-5† compares this ratio as a function of chain length between AgSCn (n = 4–16) and CuSCn (n = 4–18).[22] Our crystals present a higher conformational order than that of CuSCn lamellae at given chain lengths.

Two additional peaks observed at 2860–2875 cm^{-1} and 2950–2960 cm^{-1} belong to the symmetric (r^+) and asymmetric (r^-) stretching modes of CH_3 groups, which are irrelevant to chain conformation but are included in Table SI-III† for completeness.

Fig. 7b shows the FTIR low frequency spectra (1175–1350 cm^{-1}) of AgSCn (n = 1–16) crystals. This region of methylene wagging (W_x) mode is widely used to estimate the average number (x) of CH_2 groups in the *trans* sequence of an alkyl chain.[10,11,16,17,64,65] The inter-band spacing ($\Delta\nu$) of this progression series is measured. $\Delta\nu$ is related to x by the following equation:

$$\Delta\upsilon = \frac{326}{x+1}. \quad (3)$$

The calculated *trans* segment length, in terms of number of CH_2 units (x), for each AgSCn (n = 3–16) is plotted in Fig. 7c. The black dashed line ($x = n - 1$) represents the case where the entire chain is in *trans* conformation. It fits the experimental data well, indicating that the entire length of AgSCn (n = 3–16) chains are in *trans* conformations. This calculation is not applied to AgSC2 and AgSC1 where no *trans* configuration is defined.

A 1303 cm^{-1} peak (not shown) observed for AgSC1 is assigned to the symmetric deformation mode of CH_3.[45] A peak (not shown) at 1420 ± 3 cm^{-1} observed for all AgSCn (n = 1–16) is assigned to the deformation of S-bonded CH_2 or CH_3 groups.[57,66]

The conclusion is drawn that AgSCn (n = 4–16) lamellae synthesized in this work possess fully-extended all-*trans* alkyl chains. More details of the local structures of alkyl chains have been studied by nuclear magnetic resonance and will be the central focus of a later publication.[51]

Intralayer lattice ordering. SAED analysis is used to evaluate the degree of ordering for both intralayer and interlayer structure of this material system. To our knowledge, this is the first reported analysis for any metal–thiolates.

Fig. 8a–d selectively shows the TEM images of AgSC1, AgSC2, AgSC3 and AgSC15, respectively. Similar to the TEM images of AgSC16 reported in a previous paper,[26] all species in this work present nanosheet morphology with well-defined facets and shapes of lamellar crystals, in agreement with those observed by SEM (Fig. 3). Each flake represents a single crystalline multilayer AgSCn. The direction of the e-beam is perpendicular to the lamellar plane of (0k0) with a zone axis of [010], as shown in the inset of Fig. 8d.

This material is highly susceptible to e-beam damage. Thus we must use a short beam exposure time (<20 s) and a low beam current (~1–2 pA cm^{-2}) in order to obtain the undamaged intrinsic properties of the sample.[18] The progression of damage, which eventually leads to an amorphous SAED pattern, due to e-beam exposure is shown in Fig. SI-6.† Practically, e-beam was employed as an alternative to thermolysis[17] for decomposing metal–thiolates into metal nanoparticles.[67,68]

The presence of single crystal diffraction patterns indicates that the intralayer structures of AgSCn are highly ordered. SAED patterns taken from different locations on a certain lamellae flake exactly overlap with each other. This verifies that each nanosheet in Fig. 8 is a single crystal.

Because of the [010] zone axis, all the diffraction spots represent (h0l) planes. After appropriate image rotations, we found that the diffraction patterns of all AgSCn ($n \geq 2$, Fig. 9b–h) are identical, except for that of AgSC1. Fig. 9i denotes the labeling of eight typical spots (closest to the center of pattern) of Fig. 9b–h as A_1, A_2, B_1, B_2, C_1, C_2, D_1 and D_2. The lengths and angles of several reciprocal vectors are averaged for AgSCn

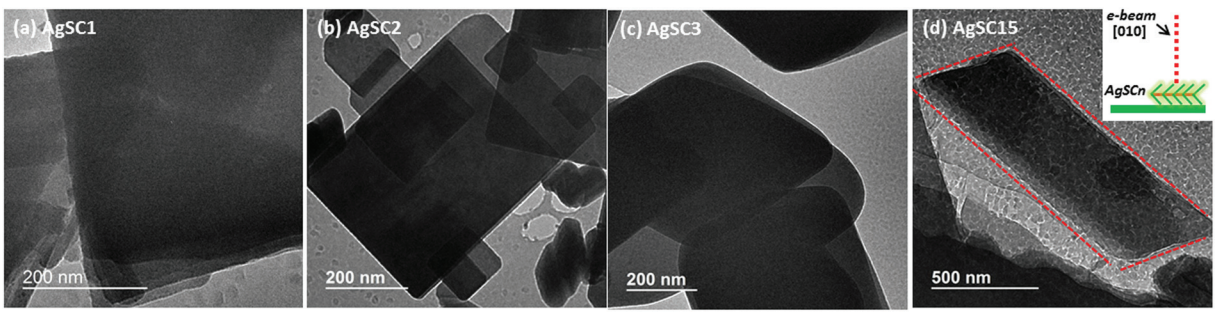

Fig. 8 (a)–(d) show the TEM images of AgSC1, AgSC2, AgSC3 and AgSC15 lamellar crystals, respectively. Morphology of single crystal nanosheets is clearly observed. The red dashed box in (d) highlights a well-shaped single crystal AgSC15. The inset of (d) illustrates the zone axis of this study is [010], which is perpendicular to the AgSCn lamellar plane of (0k0).

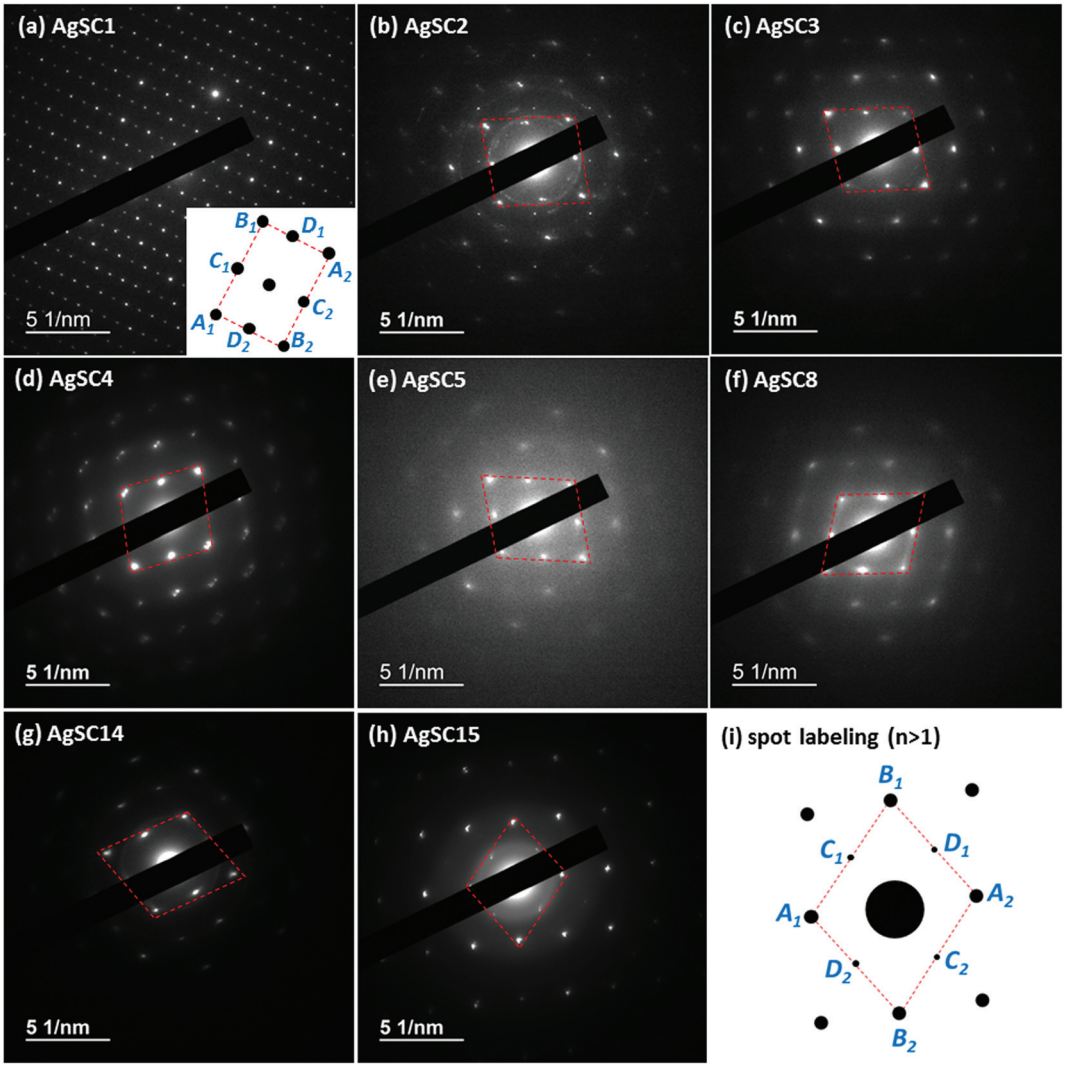

Fig. 9 (a)–(h) present the SAED patterns of AgSC*n* with n = 1, 2, 3, 4, 5, 8, 14 and 15, respectively. The zone axis is [010], as shown in Fig. 8d. The red dashed boxes in (b)–(h) help visualize the equivalence of SAED patterns for AgSC*n* (n = 2–5, 8, 14, 15). Eight typical reciprocal spots (A_1, A_2, B_1, B_2, C_1, C_2, D_1, D_2) from each pattern of (b)–(h), where $n \geq 2$, and (a) AgSC1 are labeled in the schematics shown in (i) and the inset of (a), respectively.

(n = 2–5, 8, 14, 15), presented in the second column of Table 1, with only 1–2% errors. This equivalence of ($h0l$) diffractions indicates the same intralayer lattice packing along [$h0l$] orientations for AgSC*n* ($n \geq 2$) and their central planes share a common lateral structure. This conclusion is consistent with the argument in an earlier wide-angle XRD characterization of AgSC8 and AgSC3, where the two chain-length-independent lattice parameters (a and c) of AgSC*n* were speculated to be invariant.[5]

Notably, AgSC1 shows a different SAED pattern (Fig. 9a) from the others. The dimensions of typical reciprocal vectors with an AgSC1 pattern (spot labeling shown in the inset of Fig. 9a) are presented in the third column of Table 1. These values are completely different from those averaged for the corresponding vectors with other patterns ($n \geq 2$). Thus AgSC1 possesses a unique intralayer structure with different symmetry.

The indexing of all the diffraction spots and the determination of AgSC*n* lattice are under investigation by combining SAED with synchrotron XRD analysis, and will be discussed in a later publication.[69]

Lamella thickness and layer registration. No angular breadth or arcing of high-angle spots is observed in any SAED patterns (Fig. 9a–h). This rules out the existence of a mosaic structure in the ($0k0$) plane of AgSC*n*.[70] We suggest that a sufficient translational symmetry exists in the lamellae stacked along the [010] direction and adjacent layers are well-registered. The multiple orders of reflections in the XRD patterns (Fig. 5 and SI-2†) of AgSC*n* also indicate the good registration between layers.

Layer thickness of AgSC*n* (n = 1–16) as a function of the number of CH_2 groups ($n - 1$) is plotted in Fig. 10a. This plot extends our previous layer thickness data[20] of vapor-grown (Method-2) long chain AgSC*n* to ultimately short chain

Table 1 Lengths and angles of reciprocal vectors measured from the SAED patterns of AgSC*n* ($n \geq 2$, Fig. 9b–h) and AgSC1 (Fig. 9a)

Reciprocal vectors	AgSC*n* ($n \geq 2$)	AgSC1
A_1A_2 (nm^{-1})	5.70 ± 0.12	3.01 ± 0.05
B_1B_2 (nm^{-1})	7.11 ± 0.10	2.93 ± 0.03
C_1C_2 (nm^{-1})	4.49 ± 0.06	1.66 ± 0.02
D_1D_2 (nm^{-1})	4.70 ± 0.06	2.43 ± 0.04
$\angle(A_1A_2, B_1B_2)$	85.29 ± 1.14°	68.35 ± 0.75°
$\angle(C_1C_2, D_1D_2)$	75.57 ± 1.32°	88.62 ± 0.74°

lengths. A well-resolved offset between thicknesses of odd and even chain AgSC*n* (n = 2–16) is observed (Fig. 10a and b). Since the inorganic backbone is a common segment,[5] the odd/even effect stems from the vertical packing of alkyl chains. Fijolek *et al.* reported that AgSC*n* with *gauche* defects shows different thicknesses, as compared to the crystals with fully-extended chains.[7] The linear relationship of Fig. 10a verifies that alkyl chains in AgSC*n* (n = 2–16) are similarly-extended. Considering the all-*trans* characteristic of lamellae with n = 4–16 (Fig. 7), all AgSC*n* (n = 2–16) chains are essentially fully-extended.

The two fitting lines have the same slope within experimental error (±0.01), which is defined by the fixed chain tilt angle of 18° ± 1°. This angle agrees with the one estimated from vapor-grown samples.[20] The intercept of each line equals the summation of (1) Ag–S central plane thickness, (2) twice the projection of S–C bond length (1.81 Å) along the [0*k*0] direction, and (3) the interlayer van der Waals gap,[10,16] as illustrated in Fig. SI-7.† AgSC*n* interfaces are modeled as CH_3 groups (van der Waals radius 2.00 Å) from adjacent layers bonded with hard sphere contact. The van der Waals gap is defined as the distance between the centers of two such hard spheres along the [0*k*0] direction. Since (1) and (2) are independent of chain length,[5] the 0.49 ± 0.10 Å difference between the odd and even intercepts represents the difference in the van der Waals gaps in the odd and even interfaces. The odd layers possess more densely packed interfaces. This 0.49 ± 0.10 Å difference is consistent with our prior estimation of 0.35 ± 0.13 Å obtained from vapor-grown AgSC*n*.[20]

Fittings shown in Fig. 10a are linear and parallel to each other. This implies a common lattice packing for all AgSC*n* (n = 2–16) along the vertical [0*k*0] direction. SAED analysis has suggested a common lattice packing along the lateral [*h*0*l*] directions. Thus different AgSC*n* (n = 2–16) crystals are equivalently packed in all [*hkl*] orientations and possess the same lattice type (subcell packing), except for AgSC1. Different interface packing densities and van der Waals gaps are the only differences between the odd and even lattices. Although it has been controversial regarding whether AgSC*n* possess a monoclinic,[5] orthorhombic[15] or hexagonal[8] unit cell, it is reasonable to infer that they all belong to one common lattice type, uniform for all studied chain lengths (n = 2–16) and chain parities.

In contrast, the plot of layer thickness *vs.* number of CH_2 groups (n − 2) for *n*-alkanes (C_nH_{2n+2}, n = 2–29) is shown in Fig. 10c.[71–73] Unlike Fig. 10a, the layer thickness for either odd

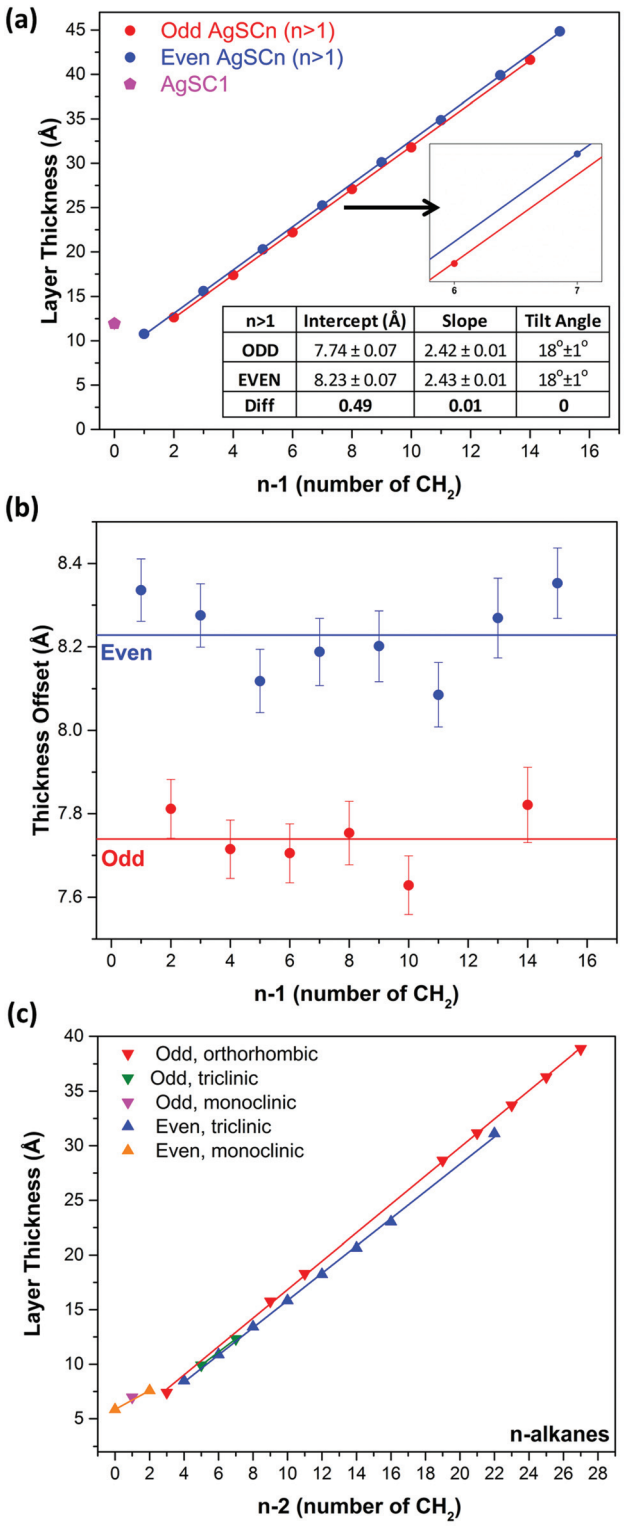

Fig. 10 (a) Plot shows layer thicknesses of AgSC*n* (n = 1–16), measured by XRD, as a function of number of CH_2 groups (n − 1). For n > 1, the data are fitted separately for odd and even chains. The inset magnifies the plot to visualize the well-resolved odd/even effect. (b) Plot shows the deviation of each data point in (a) from the linear fitting, indicating a well-resolved difference between odd and even thickness offsets. (c) Layer thickness as a function of n − 2 for *n*-alkanes.[71–73] Data with the same chain parity and same lattice packing types are fitted by single linear lines.

or even *n*-alkanes cannot be fitted by single lines and the fitted lines have different slopes. This is because different *n*-alkane lamellae belong to different lattice types. Layer thickness is determined not only by a progressive change of chain length, but also by lattice parameters, chain tilt angles and intralayer packing densities. For example, chains forming either orthorhombic or triclinic subcells are more tightly packed than chains with monoclinic or hexagonal structures.[74] Only the data of *n*-alkanes with the same lattice types can be linearly fitted, such as triclinic even alkanes with $6 \leq n \leq 24$, or orthorhombic odd alkanes with $n = 5$ and $11 \leq n \leq 29$ (Fig. 10c). Analogously, the uniqueness of AgSC1 thickness (Fig. 10a) is attributed to its particular lattice packing along the [0*k*0] direction, as compared with other AgSC*n* (n = 2–16). Such uniqueness of AgSC1 also appears laterally in [*h*0*l*] directions, revealed by its distinct SAED pattern (Fig. 9a).

Discussion

Lattice packing of aliphatic lamellae

The interlayer packing of aliphatic lamellae is determined by how interlayer interfaces are arranged. Interfaces of polyethylene (PE) lamellae are composed of amorphous CH_2 foldings that are not well-registered between adjacent layers.[75] This is consistent with the mosaic structure observed in PE crystals *via* SAED.[70,76] In contrast, interfaces of alkyl-based lamellae, such as *n*-alkanes,[71,72] metal–thiolates[20] and metal–carboxylates,[50,65,77] are well-registered, modeled as van der Waals spheres of terminal groups from slightly interpenetrating adjacent layers. Such interdigitation for AgSC*n* was estimated to be ≤0.9 Å.[20]

The layer thicknesses of $AuSC_nH_{2n+1}$,[16] $CuSC_nH_{2n+1}$ [9] and $AgO_2C(CH_2)_{n-2}CH_3$ [77,78] are reported to follow the same linear chain-length-dependent trend as AgSC*n* (n = 2–16, Fig. 10a) or *n*-alkanes of common lattice types (Fig. 10c). Such a variation is in the form of the well-known Vegard's Law,[79–81] which is only valid for layers with the same subcell packings. One distinction between *n*-alkanes and the above organometallic crystals is that more types of polymorphism are observed in *n*-alkane lamellae.

Unlike *n*-alkanes, we speculate that chain packings in metal-alkyl layers have to accommodate to the invariant networks of the rigid inorganic (M–S, M–OCO) sheets, such that lattice polymorphism tends to not occur in these lamellae. This is conceptually analogous to an "epitaxial" growth of aliphatic chains on the planar inorganic backbone. We infer that the van der Waals gaps of the metal-alkyl lamellae are larger than that of *n*-alkanes. The interface packing between metal-aliphatic layers is restricted and is not as dense as that of *n*-alkanes. Alkane lamellae only favor the unit cell packings that minimize chain energy.

Crystallographic determination of silver carboxylate lamellae that possess triclinic lattice has been completely performed using X-ray single crystal analysis.[50] However, the intralayer unit cell of metal–thiolates has been controversial for decades. Synthesis of large enough single crystal lamellae required for X-ray single crystal determination has not been reported so far. Many inferences of thiolate lattice are made only based on certain characteristic XRD or FTIR peaks,[5,10] and the conclusions are ambiguous (monoclinic,[5] orthorhombic[15] or hexagonal[8] for AgSC*n*; monoclinic or orthorhombic for CuSC*n*[22]). None of the above speculations has been confirmed, and will be discussed in detail elsewhere.[69]

Uniqueness of AgSC1

AgSC1 forms a lamellar structure. In contrast, extremely short chain $Pd(SCn)_2$ (n = 2, 3) crystals form a hexameric-ring structure,[13] which differs from their long chain counterparts that do form lamellae. We speculate that the planar Ag–S sheet is thermodynamically stable/strong enough to maintain the 2D framework of AgSC1 with chains as short as only one aliphatic group. It is the differences in the structure and stoichiometry of the inorganic backbone (Ag–S *vs.* S–Pd–S) that determine whether short chain thiolates keep a lamellar framework (AgSC*n*) or transform into other structures ($Pd(SCn)_2$).

Unlike that of AgSC*n* (n = 2–16), a unique central plane structure (Fig. 9a) and layer thickness (Fig. 10a) are observed in AgSC1 lamellae. There are two feasible reasons. (1) Prior works[5,7,8] claim that Ag atoms in the central plane can form either 2- or 3-coordinated configurations, in which Ag–S bond lengths are different (2.37 Å for digonal; 2.55 Å for trigonal). AgSC1 prefers to form an Ag–S sheet with a distinct coordination geometry from that of the others (n = 2–16), leading to a change of central plane structure and increase of layer thickness. (2) Only one CH_3 group (no CH_2 group) is attached to the Ag–S backbone of AgSC1. The chain tilt angle for AgSC1 can be changed from that of the others (18° for n = 2–16), due to the difference in steric hindrance between the CH_3 and CH_2 groups.

Dissolution of AgSC*n*

Hot toluene is so far the only known solvent that dissolves AgSC*n* crystals.[15] The different solubility of AgSC*n* in hot toluene determines whether the post-reaction processing in this work is recrystallization (n = 4, 6–16) or Ostwald ripening (n = 1–3, 5). We speculate that the dissolved species existing in solution is monolayer AgSC*n*. No direct evidence has verified this speculation. However, dilution of $Pd(SCn)_2$ solution has been employed to obtain single layer lamella, as an application of the solution exfoliation method.[23]

Dissolution of AgSC*n* is triggered by alkyl chain melting, based on the equivalence of dissolution enthalpy and melting enthalpy of long chain AgSC*n* ($n \geq 10$).[15] AgSC*n* (n = 4, 6–16) crystals with melting points ranging from 130–140 °C dissolve easily in hot toluene at 100–105 °C. Bardeau *et al.*[11] reported that AgSC12 has a pre-melting window between 100–125 °C, wherein the *gauche* CH_2 conformers start to gradually accumulate. The hot toluene temperature (100–105 °C) is just high enough to pre-melt the alkyl chains, preparing for chain reordering during the subsequent cooling for recrystallization. However, lamellae (n = 1–3, 5) with melting points (>150 °C)[51]

that are much higher than the hot toluene temperature exhibit lower solubility. Observations (see Experimental) show that the decrease of crystal solubility aligns well with the increase of lamellae melting points, in a sequence from AgSC*n* (*n* = 4, 6–16), AgSC5 to AgSC*n* (*n* = 1–3).

The maximum recrystallization temperature (100–105 °C) of AgSC*n* in hot toluene is experimentally limited by its boiling point (111 °C). Instead of toluene, we speculate that short chain AgSC*n* (*n* = 1–3, 5) might dissolve in solvents with higher boiling temperatures that are able to trigger chain melting of short chain lamellae. The melting of short chain AgSC*n* is outside the scope of this work and will be discussed elsewhere.[51]

The step-by-step nature of the recrystallization or ripening process is unknown. However, based on simple crystal growth models,[82] the size of the species involved in growth is estimated by measuring the sharpness (roughness) of the facet edges of the crystals in Fig. 8. If we assume that the facet edge is also the leading edge of crystal growth, its roughness (≤5 nm) would be the upper limit of the size of the solvated species (sheets or clusters).

Solution-grown *vs.* vapor-grown AgSC*n*

The solution-based (Method-1, Method-3) and the vapor-based (Method-2) synthesis routes for metal alkanethiolates are complementary in terms of chain length and number of layers. Method-3 in this work is capable of producing free-standing multilayer AgSC*n* with any chain lengths (*n* ≥ 1). In contrast, Method-2[18,19] grows lamellar crystals on substrates with a controllable number of layers (*m* = 1–4 or *m* ≥ 10), but has difficulty in synthesizing short chain crystals (*n* = 1–6), probably due to substrate roughness.

As compared with that of the crystals in this work (Fig. 5 and SI-2†), XRD patterns of vapor-grown AgSC*n* show much weaker and fewer (0*k*0) reflections.[18] This indicates that lamellae self-assembled on inert surfaces have poorer interlayer orderings. Their interfaces are not as well-registered as those recrystallized or ripened from hot toluene. Prior works show that some interlayer defects might exist in the interface regions of poorly ordered thiolate crystals.[38]

AgSC*n* crystals grown by Method-2 have smaller sizes than those formed from Method-3, and thus degrade faster under e-beam exposure. Special care is necessary for future SAED studies on the intralayer structures of 1-layer or a-few-layer AgSC*n*.

Conclusions

We report a systematic synthesis and characterization of a wide range of highly ordered multilayer AgSC*n* (*n* = 1–16), including both short and long chain lamellae with either chain parity.

An original modification of a solution reaction method is presented. Previously unavailable well-ordered short chain AgSC*n* (*n* = 1–6) are synthesized. All AgSC*n* species show lamellar structures with all-*trans* alkyl chains attached to the Ag–S backbone. AgSC2 (1.08 nm) is the thinnest organometallic layer ever reported. Hot toluene recrystallization or Ostwald ripening improves the interlayer and intralayer orderings of the lamellae. All AgSC*n* decompose into a mixture of Ag and Ag_2S beyond 210 °C.

The multilayer lamellae synthesized in this work are verified to be single crystals with well-registered interlayer interfaces, even for extremely short chain AgSC*n* (*n* = 1–3). Unlike *n*-alkane lamellae that show many types of subcell packing, all AgSC*n* (*n* = 2–16) possess a common central plane structure and the same lattice packing, except for AgSC1, whose layer thickness does not follow the linear Vegard's Law of the others. The lack of polymorphism in the AgSC*n* (*n* = 2–16) lattice, as compared with that of *n*-alkanes, arises from the accommodation of the aliphatic chain packing to the rigid inorganic network.

Acknowledgements

This work is supported by NSF-DMR-1409953 and NSF-DMR-1006385. Material characterization was carried out in the Frederick Seitz Materials Research Laboratory, the School of Chemical Sciences Facilities, and the Ceramics Kiln House, University of Illinois, Urbana-Champaign. The authors thank Ms N. Robards for the help with DSC measurements.

References

1 A. K. Geim and K. S. Novoselov, *Nat. Mater.*, 2007, **6**, 183–191.
2 M. Y. Efremov, F. Schiettekatte, M. Zhang, E. A. Olson, A. T. Kwan, R. S. Berry and L. H. Allen, *Phys. Rev. Lett.*, 2000, **85**, 3560–3563.
3 M. Zhang, M. Y. Efremov, F. Schiettekatte, E. A. Olson, A. T. Kwan, S. L. Lai, T. Wisleder, J. E. Greene and L. H. Allen, *Phys. Rev. B: Condens. Matter*, 2000, **62**, 10548–10557.
4 H. S. Nalwa, *Handbook of Thin Film Materials: Nanomaterials and magnetic thin films*, Academic Press, 2002.
5 I. G. Dance, K. J. Fisher, R. M. H. Banda and M. L. Scudder, *Inorg. Chem.*, 1991, **30**, 183–187.
6 M. J. Baena, P. Espinet, M. C. Lequerica and A. M. Levelut, *J. Am. Chem. Soc.*, 1992, **114**, 4182–4185.
7 H. G. Fijolek, J. R. Grohal, J. L. Sample and M. J. Natan, *Inorg. Chem.*, 1997, **36**, 622–628.
8 F. Bensebaa, T. H. Ellis, E. Kruus, R. Voicu and Y. Zhou, *Langmuir*, 1998, **14**, 6579–6587.
9 P. Espinet, M. C. Lequerica and J. M. Martín-Alvarez, *Chem. – Eur. J.*, 1999, **5**, 1982–1986.
10 A. N. Parikh, S. D. Gillmor, J. D. Beers, K. M. Beardmore, R. W. Cutts and B. I. Swanson, *J. Phys. Chem. B*, 1999, **103**, 2850–2861.

11 J.-F. O. Bardeau, A. N. Parikh, J. D. Beers and B. I. Swanson, *J. Phys. Chem. B*, 2000, **104**, 627–635.
12 R. Voicu, A. Badia, F. Morin, R. B. Lennox and T. H. Ellis, *Chem. Mater.*, 2000, **12**, 2646–2652.
13 P. J. Thomas, A. Lavanya, V. Sabareesh and G. U. Kulkarni, *J. Chem. Sci.*, 2001, **113**, 611–619.
14 R. Voicu, A. Badia, F. Morin, R. B. Lennox and T. H. Ellis, *Chem. Mater.*, 2001, **13**, 2266–2271.
15 A. A. Levchenko, C. K. Yee, A. N. Parikh and A. Navrotsky, *Chem. Mater.*, 2005, **17**, 5428–5438.
16 S.-H. Cha, J.-U. Kim, K.-H. Kim and J.-C. Lee, *Chem. Mater.*, 2007, **19**, 6297–6303.
17 S.-H. Cha, K.-H. Kim, J.-U. Kim, W.-K. Lee and J.-C. Lee, *J. Phys. Chem. C*, 2008, **112**, 13862–13868.
18 L. Hu, Z. S. Zhang, M. Zhang, M. Y. Efremov, E. A. Olson, L. P. de la Rama, R. K. Kummamuru and L. H. Allen, *Langmuir*, 2009, **25**, 9585–9595.
19 L. Hu, L. P. de la Rama, M. Y. Efremov, Y. Anahory, F. Schiettekatte and L. H. Allen, *J. Am. Chem. Soc.*, 2011, **133**, 4367–4376.
20 L. P. de la Rama, L. Hu, Z. Ye, M. Y. Efremov and L. H. Allen, *J. Am. Chem. Soc.*, 2013, **135**, 14286–14298.
21 Z. Ye, L. P. de la Rama, L. Hu, M. Y. Efremov and L. H. Allen, *Thermochim. Acta*, 2015, **603**, 69–78.
22 N. Sandhyarani and T. Pradeep, *J. Mater. Chem.*, 2001, **11**, 1294–1299.
23 B. Busupalli, S. Kummara, G. Kumaraswamy and B. L. V. Prasad, *Chem. Mater.*, 2014, **26**, 3436–3442.
24 N. S. John, G. U. Kulkarni, A. Datta, S. K. Pati, F. Komori, G. Kavitha, C. Narayana and M. K. Sanyal, *J. Phys. Chem. C*, 2007, **111**, 1868–1870.
25 B. Pokroy, B. Aichmayer, A. S. Schenk, B. Haimov, S. H. Kang, P. Fratzl and J. Aizenberg, *J. Am. Chem. Soc.*, 2010, **132**, 14355–14357.
26 J. Garcia-Barrasa, J. M. Lopez-de-Luzuriaga, M. Monge, K. Soulantica and G. Viau, *J. Nanopart. Res.*, 2011, **13**, 791–801.
27 J. Duan, J. Ma, B. Wu, Q. Li, J. Fang and D. Chen, *J. Mater. Chem. C*, 2014, **2**, 2375–2386.
28 X. Jia, J. Li and E. Wang, *Chem. Commun.*, 2014, **50**, 9565–9568.
29 A. Badia, R. B. Lennox and L. Reven, *Acc. Chem. Res.*, 2000, **33**, 475–481.
30 Z. S. Zhang, O. M. Wilson, M. Y. Efremov, E. A. Olson, P. V. Braun, W. Senaratne, C. K. Ober, M. Zhang and L. H. Allen, *Appl. Phys. Lett.*, 2004, **84**, 5198.
31 J. C. Love, L. A. Estroff, J. K. Kriebel, R. G. Nuzzo and G. M. Whitesides, *Chem. Rev.*, 2005, **105**, 1103–1170.
32 R. T. W. Popoff, K. L. Kavanagh and H.-Z. Yu, *Nanoscale*, 2011, **3**, 1434–1445.
33 R. T. W. Popoff, A. A. Zavareh, K. L. Kavanagh and H.-Z. Yu, *J. Phys. Chem. C*, 2012, **116**, 17040–17047.
34 A. Badia, W. Gao, S. Singh, L. Demers, L. Cuccia and L. Reven, *Langmuir*, 1996, **12**, 1262–1269.
35 A. Badia, S. Singh, L. Demers, L. Cuccia, G. R. Brown and R. B. Lennox, *Chem. – Eur. J.*, 1996, **2**, 359–363.
36 A. Badia, L. Demers, L. Dickinson, F. G. Morin, R. B. Lennox and L. Reven, *J. Am. Chem. Soc.*, 1997, **119**, 11104–11105.
37 P. D. Jadzinsky, G. Calero, C. J. Ackerson, D. A. Bushnell and R. D. Kornberg, *Science*, 2007, **318**, 430–433.
38 B. Radha, G. Liu, D. J. Eichelsdoerfer, G. U. Kulkarni and C. A. Mirkin, *ACS Nano*, 2013, **7**, 2602–2609.
39 N. S. John, S. K. Pati and G. U. Kulkarni, *Appl. Phys. Lett.*, 2008, **92**, 013120.
40 H. Mohwald, *Annu. Rev. Phys. Chem.*, 1990, **41**, 441–476.
41 Q. H. Wang, K. Kalantar-Zadeh, A. Kis, J. N. Coleman and M. S. Strano, *Nat. Nanotechnol.*, 2012, **7**, 699–712.
42 S. Z. Butler, S. M. Hollen, L. Cao, Y. Cui, J. A. Gupta, H. R. Gutiérrez, T. F. Heinz, S. S. Hong, J. Huang, A. F. Ismach, E. Johnston-Halperin, M. Kuno, V. V. Plashnitsa, R. D. Robinson, R. S. Ruoff, S. Salahuddin, J. Shan, L. Shi, M. G. Spencer, M. Terrones, W. Windl and J. E. Goldberger, *ACS Nano*, 2013, **7**, 2898–2926.
43 K. F. Mak, C. Lee, J. Hone, J. Shan and T. F. Heinz, *Phys. Rev. Lett.*, 2010, **105**, 136805.
44 S. S. Hong, W. Kundhikanjana, J. J. Cha, K. Lai, D. Kong, S. Meister, M. A. Kelly, Z.-X. Shen and Y. Cui, *Nano Lett.*, 2010, **10**, 3118–3122.
45 S. B. Lee, K. Kim, M. S. Kim, W. S. Oh and Y. S. Lee, *J. Mol. Struct.*, 1993, **296**, 5–13.
46 B. E. Warren, *X-ray diffraction*, Dover Publications, New York, 1990.
47 B. Vidal and P. Vincent, *Appl. Opt.*, 1984, **23**, 1794–1801.
48 J. P. Locquet, D. Neerinck, L. Stockman, Y. Bruynseraede and I. K. Schuller, *Phys. Rev. B: Condens. Matter*, 1989, **39**, 13338–13342.
49 E. E. Fullerton, I. K. Schuller, H. Vanderstraeten and Y. Bruynseraede, *Phys. Rev. B: Condens. Matter*, 1992, **45**, 9292–9310.
50 L. P. Olson, D. R. Whitcomb, M. Rajeswaran, T. N. Blanton and B. J. Stwertka, *Chem. Mater.*, 2006, **18**, 1667–1674.
51 Z. Ye, L. P. de la Rama, M. Y. Efremov, A. Sutrisno and L. H. Allen, manuscript in preparation, 2016.
52 F. Grønvold and E. F. Westrum, *J. Chem. Thermodyn.*, 1986, **18**, 381–401.
53 G. A. Martínez-Castañón, M. G. Sánchez-Loredo, H. J. Dorantes, J. R. Martínez-Mendoza, G. Ortega-Zarzosa and F. Ruiz, *Mater. Lett.*, 2005, **59**, 529–534.
54 S. I. Sadovnikov, A. I. Gusev and A. A. Rempel, *Phys. Chem. Chem. Phys.*, 2015, **17**, 20495–20501.
55 R. G. Nuzzo, F. A. Fusco and D. L. Allara, *J. Am. Chem. Soc.*, 1987, **109**, 2358–2368.
56 L. H. Dubois and R. G. Nuzzo, *Annu. Rev. Phys. Chem.*, 1992, **43**, 437–463.
57 M. J. Hostetler, J. J. Stokes and R. W. Murray, *Langmuir*, 1996, **12**, 3604–3612.
58 R. A. MacPhail, H. L. Strauss, R. G. Snyder and C. A. Elliger, *J. Phys. Chem.*, 1984, **88**, 334–341.
59 H. J. Choi, S. W. Han, S. J. Lee and K. Kim, *J. Colloid Interface Sci.*, 2003, **264**, 458–466.
60 S.-H. Park and C. E. Lee, *Chem. Mater.*, 2006, **18**, 981–987.

61 M. Maroncelli, S. P. Qi, H. L. Strauss and R. G. Snyder, *J. Am. Chem. Soc.*, 1982, **104**, 6237–6247.
62 R. G. Snyder, H. L. Strauss and C. A. Elliger, *J. Phys. Chem.*, 1982, **86**, 5145–5150.
63 N. Sandhyarani, M. P. Antony, G. P. Selvam and T. Pradeep, *J. Chem. Phys.*, 2000, **113**, 9794–9803.
64 R. G. Snyder and J. H. Schachtschneider, *Spectrochim. Acta*, 1963, **19**, 85–116.
65 S. J. Lee, S. W. Han, H. J. Choi and K. Kim, *J. Phys. Chem. B*, 2002, **106**, 2892–2900.
66 R. N. A. H. Lewis and R. N. McElhaney, *Biochim. Biophys. Acta*, 2013, **1828**, 2347–2358.
67 J.-U. Kim, S.-H. Cha, K. Shin, J. Y. Jho and J.-C. Lee, *J. Am. Chem. Soc.*, 2005, **127**, 9962–9963.
68 S.-E. Kim, Y.-H. Han, B. c. Lee and J.-C. Lee, *Nanotechnology*, 2010, **21**, 075302.
69 Z. Ye, M. Y. Efremov, K. C. Seymour, W. M. Kriven, J.-M. Zuo and L. H. Allen, manuscript in preparation, 2016.
70 D. Dorset, *Acta Crystallogr., Sect. A: Cryst. Phys., Diffr., Theor. Gen. Cryst.*, 1976, **32**, 207–215.
71 D. M. Small, *The physical chemistry of lipids: from alkanes to phospholipids*, Plenum Press, New York, 2nd edn, 1986.
72 R. Boese, H.-C. Weiss and D. Blaser, *Angew. Chem., Int. Ed.*, 1999, **38**, 988–992.
73 D. L. Dorset, *Crystallography of the Polymethylene Chain*, Oxford University Press, New York, 1st edn, 2005.
74 D. M. Small, *J. Lipid Res.*, 1984, **25**, 1490–1500.
75 S. Rastogi, A. B. Spoelstra, J. G. P. Goossens and P. J. Lemstra, *Macromolecules*, 1997, **30**, 7880–7889.
76 A. T. Kwan, M. Efremov, E. A. Olson, F. Schiettekatte, M. Zhang, P. H. Geil and L. H. Allen, *J. Polym. Sci., Part B: Polym. Phys.*, 2001, **39**, 1237–1245.
77 P. N. Nelson and H. A. Ellis, *Dalton Trans.*, 2012, **41**, 2632–2638.
78 K. Binnemans, R. Van Deun, B. Thijs, I. Vanwelkenhuysen and I. Geuens, *Chem. Mater.*, 2004, **16**, 2021–2027.
79 A. R. Denton and N. W. Ashcroft, *Phys. Rev. A*, 1991, **43**, 3161–3164.
80 H. Wei, M. Li, Z. Ye, Z. Yang and Y. Zhang, *Mater. Lett.*, 2011, **65**, 427–429.
81 H. Wei, Z. Ye, M. Li, Y. Su, Z. Yang and Y. Zhang, *CrystEngComm*, 2011, **13**, 2222–2226.
82 C. L. Andrea and K. Miroslav, *J. Phys.: Condens. Matter*, 1997, **9**, 299.